NPC-Based Multi-Source Inverters for Multimode DC Rail Traction Systems

Emanuele Fedele, Diego Iannuzzi, Pietro Tricoli, *Member, IEEE*, and Andrea Del Pizzo, *Member, IEEE*

***Abstract*— The need for decarbonization has increased the interest in alternative propulsion systems for light rail vehicles, including fuel cells, batteries, and supercapacitors. These sources and storage devices can also be used in combination with an external supply to enable operation on both electrified and nonelectrified tracks. In traditional architectures, the sources are connected via dc/dc converters to a common dc-link that feeds the motor drives. This article addresses a new configuration where an NPC-based multisource inverter (MSI) is used for the integration of the dc sources to the traction motors in a single stage. First, a thorough analysis of the converter's operation is carried out with reference to its state-of-the-art control. The conditions for full control of the dc sources and traction motors over the entire vehicle speed profile are derived. Second, a novel modulation technique is proposed to complement the baseline control and enable the stationary charging of the energy storage from the electrified line through the converter. Thus, the MSI can be operated to match all the functionalities of conventional multimode architecture, with the advantage of the reduced number of power converters. Validations are carried out by means of simulations and extensive experiments on a laboratory test bench.**

***Index Terms*— Energy storage systems (ESSs), hybrid powertrains, light rail vehicles (LRVs), multimode rail traction systems, multisource inverter (MSI).**

I. Introduction

DURING the last decade, light rail vehicles (LRVs) have increasingly used energy storage devices (i.e., batteries and supercapacitors) and alternative primary sources (i.e., fuel cells) to meet transport decarbonization targets [1]–[3]. The combination of energy storage devices and/or alternative sources to the main power supply results in a multimode powertrain, for which the same vehicle performance can be obtained with a higher energy and power densities if the sources are optimally managed [4]–[7]. For simplicity, the term power source shall be used in the following for both the electrified line supply and onboard storage devices.

Manuscript received 17 January 2022; revised 10 April 2022; accepted 10 May 2022. Date of publication 13 May 2022; date of current version 21 February 2023. This work was supported by the program PON "Ricerca e Innovazione" 2014-2020, Azione I.1: "Dottorati Innovativi con Caratterizzazione Industriale," under Project DOT1318930, CUP E65F19001220007, funded by the Italian Ministry of University and Research (MUR). *(Corresponding author: Emanuele Fedele.)*

Emanuele Fedele, Diego Iannuzzi, and Andrea Del Pizzo are with the Department of Electrical Engineering and Information Technology (DIETI), Università degli Studi di Napoli Federico II, 80125 Naples, Italy (e-mail: emanuele.fedele@unina.it; iandiego@unina.it; delpizzo@unina.it).

Pietro Tricoli is with the Department of Electronic, Electrical and Systems Engineering, University of Birmingham, Birmingham B15 2TT, U.K. (e-mail: p.tricoli@bham.ac.uk).

Digital Object Identifier 10.1109/TTE.2022.3175097

All multimode traction architectures feature power converters to interconnect the power sources and control the energy flows [8]–[16]. Traditionally, trainborne power sources are connected to a common dc-link through a dc/dc converter, with the dc-link feeding each traction inverter for either one or two traction motors [11]–[13], [17]. Minimizing the rating of the dc/dc converter is required to reduce the cost, weight, and size of the traction system. In fact, the converter has to be designed for the peak power of the input source and typically requires large magnetic components, which determines a major share of its volume and weight [18]. More compact solutions for the power converters can be achieved by downsizing the heat sinks and filters. A major trend to reduce the size of heat sinks and passive filters is based on the use of wide bandgap power semiconductors [19]–[21]. Other approaches have focused on alternative topologies to reduce or eliminate magnetics or capacitors, such as modular multilevel converters [22]–[25], partial-power-processing concepts [26], [27], bidirectional choppers with auxiliary converters [18], [28], dual-input two-level inverter topologies [29]–[31], and NPC-based multisource inverters (MSIs) [32]–[37].

MSIs based on the NPC topology (in the following, MSIs) allow a single-stage interconnection of multiple dc sources to the same ac load without magnetic elements through a conventional NPC circuit. An MSI architecture is presented in [32] for hybrid automotive powertrains. The topology enables the dc sources to provide two different output voltage levels and feed the traction motor independently, thus removing the need for additional dc/dc converters. The potential benefits of an MSI-based topology for hybrid power-split powertrains are further analyzed in [34], where new powertrain control modes are proposed to consider the MSI characteristics and allow for a VA-rating reduction of the main dc/dc converter. Salari *et al.* [35] propose a reconfigurable topology of the MSI, where the reconfigurability is achieved by introducing two additional switches to the original circuit configuration. The main advantage of this configuration is supplying the motor with an overall dc voltage that is the sum of the source voltages. In [36], a similar MSI topology and a control approach are analyzed to integrate the power converter of the energy storage device with the motor drive of a tramway vehicle. Two standard VSIs in parallel are fed by the main supply source and the energy storage device, respectively. This configuration reduces weight and device count compared with traditional topologies employing dc/dc converters and does not require modifications to the traction motors. However, the two

dc sources may frequently operate at significantly different voltage levels, and the effect of such voltage unbalance on the overall performance of the traction drive was not addressed in the study. Dorn-Gomba *et al.* [33] propose a simple current-sharing control (CSC) to actively manage the current distribution between two dc sources supplying the MSI. This control discharges one source at a time and periodically switches between sources to maintain a smooth current sharing between them. However, a controlled recharge of one source from the other through the MSI cannot be achieved by the proposed control, resulting in a significant performance deficit for the converter.

Most of the available contributions on the MSI deal with hybrid-electric automotive powertrains, where the battery is the only source of the traction circuit, while the electric motor is mechanically coupled to the combustion engine. The resulting operating modes and management strategies are focused on the specific characteristics of these sources and automotive applications. On the other hand, multimode rail vehicles are supplied by two or more independent electrical sources, one of them being either the overhead line or a fuel cell. On rail vehicles, the energy management strategy (EMS) requires that the onboard energy storage delivers a share of the traction power during acceleration and recovers most of the train kinetic energy during braking. Moreover, the storage device is charged from the catenary during stops at stations or at depots.

To evaluate the competitiveness of MSIs for traction circuits of multimode rail vehicles, two important questions must be addressed.

1) What is the performance of the MSI CSC and which system parameters affect the conditions for full control of the dc sources and the motor drives?
2) Is it possible to derive an alternative modulation strategy that allows the MSI to charge the energy storage from the external power supply when the vehicle is stationary?

To answer the first question, a thorough theoretical analysis of the MSI operation is developed. The analysis reveals that, among three possible working conditions, only one enables the MSI to fully control the power-sharing between dc sources while correctly supplying the traction motors. The relation between these conditions and the system parameters is highlighted to identify the design constraints that prevent the MSI from an uncontrolled operation. The second question is addressed by proposing a novel modulation strategy that operates the MSI as a bidirectional dc/dc converter by using the motor windings as boost inductors. The modulation effectively allows controlling the recharging of the energy storage system (ESS) from the electrified line and, thus, extends the MSI functionalities to match all those of standard traction circuits for rail vehicles supplied by multiple sources.

The remainder of this article is structured as follows. The MSI-based topology for multimode rail traction circuits is introduced in Section II. A thorough theoretical analysis of the converter under the operation of the CSC is presented in Section III. A novel modulation strategy for stationary recharge control is proposed and discussed in Section IV. The results of extensive experimental tests are presented in Section V. Conclusions are drawn in Section VI.

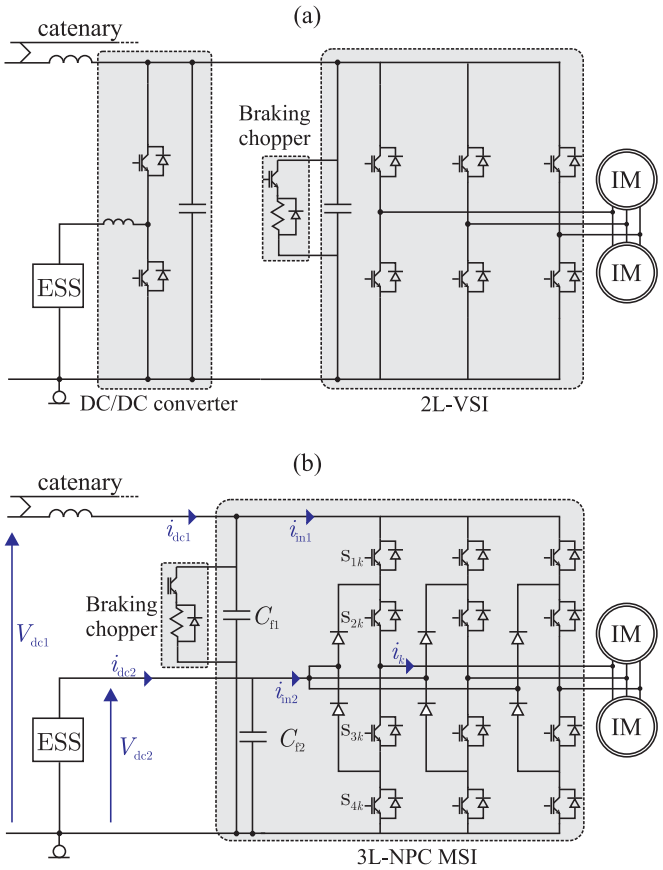

Fig. 1. Traction circuit of an LRV with 750-V overhead supply and onboard ESS: (a) conventional semi-active topology with VSI and dc/dc converter and (b) alternative single-stage topology with the 3L NPC-based MSI.

II. Multisource Inverter for Multimode Rail Traction Circuits

ESSs are adopted onboard LRVs to enable partial or complete catenary-free operation, increase the kinetic energy recovery during braking, and reduce the current drawn from the electrified line during acceleration. In electrified 600/750 VDC LRVs, the dc line feeds directly to the traction converters, while ESS are connected to the system bus through dc/dc converters, as shown in Fig. 1(a). The dc/dc converter adapts the voltage of the storage device to the dc line and enables the current control of the ESS. Such flexibility is obtained at the expense of extra semiconductor devices and a high-power inductor. Interleaved dc/dc converters with multiple legs are often employed to partly reduce the size of magnetics, at the price of increased system complexity.

NPC inverters in standard configuration are already proposed by some manufacturers [38] as traction converters for 1.5-/3-kV dc and 15-/25-kV ac regional and suburban trains. For multimode LRVs, the NPC converter can be used as an MSI to replace the dc/dc converter and the inverter, as depicted in Fig. 1(b). The NPC converter is responsible for the control of traction motors and for the energy management of the dc sources. Specifically, the MSI must be able to do the following.

1) Share the load power during traction mode with a controllable contribution of the ESS, and recover the maximum amount of kinetic energy in the ESS during braking.

TABLE I
MSI CONDUCTION MODES AND SWITCHING STATES

MSI conduction mode	NPC leg switching state				Leg output voltage
	s_{1k}	s_{2k}	s_{3k}	s_{4k}	$V_{k\mathrm{N}}$
LVO	1	1	0	0	V_{dc1}
AS	0	1	1	0	V_{dc2}
HVO	0	0	1	1	0

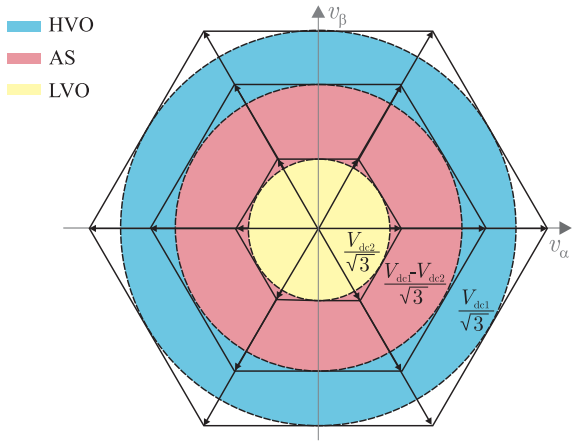

Fig. 2. MSI space vector diagram comprising three hexagons (one for each dc input voltage), 18 active vectors, and one zero vector.

2) Charge the ESS from the electrified line when the LRV stops.

The first functionality is undertaken by the state-of-the-art CSC of the MSI, while the stationary charging is achieved by a modified modulation strategy presented in this article. Both control techniques are discussed extensively in the following sections.

III. ANALYSIS OF THE POWER-SHARING CONTROL

A. Principle of Operation

When operated as MSI, the 3L-NPC converter is conceived as three 2L inverters integrated into one circuit. As shown in Table I, only two groups of switches are activated during each modulation interval, while the third group is kept in the OFF-state [34]. Depending on the active switches, three conduction modes can be identified.

1) *Low-Voltage-Only (LVO) Conduction Mode:* The load is supplied by ESS, while the overhead supply is disconnected.
2) *Antiseries (AS) Conduction Mode:* The load is supplied by the AS connection of the line with the ESS.
3) *High-Voltage-Only (HVO) Conduction Mode:* The load is supplied by the catenary, while the ESS is disconnected.

This modulation approach results in three hexagons and 19 active voltage vectors in the $\alpha\beta$ plane, as shown in Fig. 2. After the conduction mode and sector are identified, standard space vector modulation (SVM) techniques can be applied.

To control the distribution of load power between sources through an NPC-based MSI, a CSC strategy has been proposed in [33]. According to this strategy, a fixed time window of length T_{cs} and a corresponding duty cycle d_{cs} are introduced.

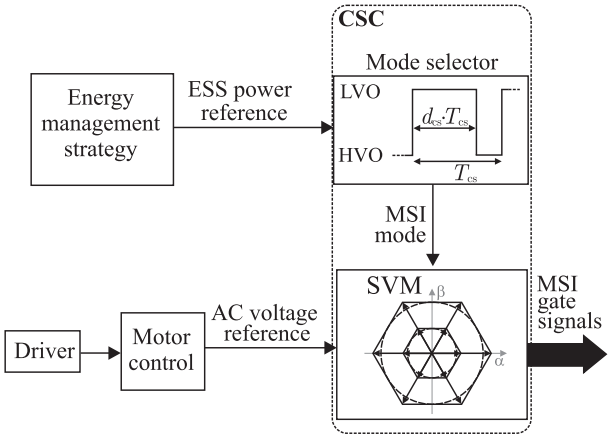

Fig. 3. Integration of the CSC with the control layers of motors and dc sources.

Within this window, the MSI is operated alternatively in LVO and HVO modes for a duration equal to $d_{\mathrm{cs}}T_{\mathrm{cs}}$ and $(1-d_{\mathrm{cs}})T_{\mathrm{cs}}$, respectively (AS conduction mode is not used). The CSC duty cycle determines the distribution of average load power between dc sources. In each conduction mode, SVM is applied to the corresponding modulation area of the space vector diagram to generate the desired ac voltages. The integration of the CSC with the motor control and dc sources energy management is represented by the block diagram of Fig. 3. The motor control layer takes the driver inputs to compute the motor reference voltages, while the energy management sets the ESS power setpoint. The two reference signals are jointly used by the CSC algorithm to set the relative duration of LVO and HVO modes and drive the MSI components accordingly.

The features, operating limits, and conditions for full control of the traction drives and dc sources can be identified by deriving the equations that govern the MSI behavior under CSC operation.

B. Mathematical Model

By coding the CSC action with the square-wave control signal

$$u_{\mathrm{cs}} = \begin{cases} 1, & \text{in LVO mode} \\ 0, & \text{in HVO mode} \end{cases} \tag{1}$$

the following power balance equations can be written:

$$V_{\mathrm{dc1}} i_{\mathrm{in1}} = (1-u_{\mathrm{cs}}) \sum_{k=1}^{3} v_k i_k \tag{2a}$$

$$V_{\mathrm{dc2}} i_{\mathrm{in2}} = u_{\mathrm{cs}} \sum_{k=1}^{3} v_k i_k \tag{2b}$$

where v_k and i_k are the instantaneous ac phase voltages and currents, and the sum of their products represents the ac output power. By considering the semiconductors as ideal switches and supposing that the motor is in steady-state symmetrical operation, the output power can be expressed as $3\,V_{\mathrm{ph}} I_{\mathrm{ph}} \cos\varphi$, where $\cos\varphi$ is the load power factor, and V_{ph} and I_{ph} are the rms values of the motor phase voltages and currents over a

time window of short duration compared with the mechanical time constants of the motor. The electrical steady-state assumption can be justified in view of the high inertia train, which results in mechanical transients being slower than electrical transients. Therefore, a dynamic operation of the traction drive can be approximated as a succession of conditions of local electrical steady state. The phase voltage can be related to the dc voltages through two indexes m_{HV} and m_{LV} defined as

$$\sqrt{2}V_{\mathrm{ph}} = \begin{cases} m_{\mathrm{HV}}\dfrac{V_{\mathrm{dc1}}}{\sqrt{3}}, & \text{in HVO mode} \\ m_{\mathrm{LV}}\dfrac{V_{\mathrm{dc2}}}{\sqrt{3}}, & \text{in LVO mode.} \end{cases} \tag{3}$$

By arranging (2a) and (2b) to make the modulation indexes explicit, one derives

$$i_{\mathrm{in1}} = \sqrt{3/2}\,(1-u_{\mathrm{cs}})m_{\mathrm{HV}}I_{\mathrm{ph}}\cos\varphi \tag{4a}$$

$$i_{\mathrm{in2}} = \sqrt{3/2}\,u_{\mathrm{cs}}m_{\mathrm{LV}}I_{\mathrm{ph}}\cos\varphi. \tag{4b}$$

By averaging (4a) and (4b) over one CSC period and assuming that all the ripple components of i_{in1} and i_{in2} flow in the dc capacitors, the dc source currents can be calculated as

$$i_{\mathrm{dc1}} = \sqrt{3/2}\,(1-d_{\mathrm{cs}})m_{\mathrm{HV}}I_{\mathrm{ph}}\cos\varphi \tag{5a}$$

$$i_{\mathrm{dc2}} = \sqrt{3/2}\,d_{\mathrm{cs}}m_{\mathrm{LV}}I_{\mathrm{ph}}\cos\varphi. \tag{5b}$$

Equations (5a) and (5b) explicitly relate the currents supplied by the dc sources to the CSC duty cycle and modulation indexes. The relation governing their ratio can be then derived

$$\frac{i_{\mathrm{dc2}}}{i_{\mathrm{dc1}}} = \frac{m_{\mathrm{LV}}}{m_{\mathrm{HV}}}\frac{d_{\mathrm{cs}}}{(1-d_{\mathrm{cs}})}. \tag{6}$$

The current split between dc sources depends not only on the duty cycle d_{cs} but also on the modulation indexes. The quantity d_{cs} represents a degree of freedom, whereas the modulation indexes depend on the motor voltage and, thus, are mainly proportional to its speed (in the constant-torque operating area). The average MSI output voltage over one CSC period can be obtained from (1) and (3) as

$$V_{\mathrm{ph}} = m_{\mathrm{HV}}\frac{V_{\mathrm{dc1}}}{\sqrt{6}}(1-d_{\mathrm{cs}}) + m_{\mathrm{LV}}\frac{V_{\mathrm{dc2}}}{\sqrt{6}}d_{\mathrm{cs}}. \tag{7}$$

Ultimately, by multiplying both sides of (5a) and (5b) with V_{dc1} and V_{dc2}, respectively, and using (3), the average power balance between dc sources and ac output is derived

$$V_{\mathrm{dc1}}i_{\mathrm{dc1}} = (1-d_{\mathrm{cs}})\,3V_{\mathrm{ph}}I_{\mathrm{ph}}\cos\varphi \tag{8a}$$

$$V_{\mathrm{dc2}}i_{\mathrm{dc2}} = d_{\mathrm{cs}}\,3\;V_{\mathrm{ph}}I_{\mathrm{ph}}\cos\varphi. \tag{8b}$$

Equation (8b) is used to determine the value of d_{cs} based on the power drawn by the load and the required dc power output.

C. Operating Conditions and Limits

The limit of linear modulation may be reached during LVO and HVO modes depending on the magnitudes of the motor voltage reference and the dc input voltages. Considering the space vector of the reference motor voltage $\boldsymbol{v}_s$ and the $\alpha\beta$ SVM plane in Fig. 2, three conditions can occur.

1) $\boldsymbol{v}_s$ lays inside the inner circle of the hexagon associated with V_{dc2}: the MSI is operated in linear modulation during both HVO and LVO, that is, $m_{\mathrm{HV}} < m_{\mathrm{LV}} < 1$.
2) $\boldsymbol{v}_s$ lays outside the inner circle associated with V_{dc2} but within the larger circle associated with V_{dc1}: the MSI is at the limit of linear modulation during LVO mode and in linear modulation during the HVO mode, that is, $m_{\mathrm{HV}} < m_{\mathrm{LV}} = 1$.
3) $\boldsymbol{v}_s$ lays outside the larger inner circle associated with V_{dc1}: the MSI always works at the limit of linear modulation, that is, $m_{\mathrm{HV}} = m_{\mathrm{LV}} = 1$.

Condition A allows a stable operation of the MSI drive and full control on the current split between dc sources. In fact, as both modulation indexes are below unity, their ratio can be related to the ratio of the dc input voltages through (3)

$$\left.\frac{m_{\mathrm{LV}}}{m_{\mathrm{HV}}}\right|_A = \frac{V_{\mathrm{dc1}}}{V_{\mathrm{dc2}}}. \tag{9}$$

By substituting the above relation into (6), the following relation for the dc currents split with the MSI in condition A results:

$$\left.\frac{i_{\mathrm{dc2}}}{i_{\mathrm{dc1}}}\right|_A = \frac{V_{\mathrm{dc1}}}{V_{\mathrm{dc2}}}\frac{d_{\mathrm{cs}}}{(1-d_{\mathrm{cs}})}. \tag{10}$$

Equation (10) allows setting the proper duty cycle to achieve a predefined load current split between dc sources.

In condition B, the modulation index m_{LV} saturates to unity. During LVO mode, the MSI operates at the limit of linear modulation, and the actual voltage output has a lower magnitude than its reference, which results in the motor currents starting to drift from their reference. Nevertheless, as the HVO conduction mode is entered, a higher dc voltage level enables the MSI to regain control of the currents. This means that the overall average phase voltage

$$V_{\mathrm{ph}}\big|_B = m_{\mathrm{HV}}\frac{V_{\mathrm{dc1}}}{\sqrt{6}}(1-d_{\mathrm{cs}}) + \frac{V_{\mathrm{dc2}}}{\sqrt{6}}d_{\mathrm{cs}} \tag{11}$$

is still sufficient for the motor to work properly and develop full torque. However, due to this dynamic, a high ripple at CSC frequency f_{cs} will appear in the ac currents. Furthermore, the load current split between sources is no more controllable by acting on the CSC duty cycle. In fact, by specializing (6) to the case $m_{\mathrm{LV}} = 1$, one derives

$$\left.\frac{i_{\mathrm{dc2}}}{i_{\mathrm{dc1}}}\right|_B = \frac{1}{m_{\mathrm{HV}}}\frac{d_{\mathrm{cs}}}{(1-d_{\mathrm{cs}})} \propto \frac{1}{\omega_r}\frac{d_{\mathrm{cs}}}{(1-d_{\mathrm{cs}})} \tag{12}$$

where the last relation holds true since the motor phase voltages increase with speed, and so does the modulation index of the high-voltage source. Therefore, for a fixed CSC duty cycle, the current split between dc sources is no longer constant but decreases with speed. By imposing $m_{\mathrm{LV}} = 1$ in (5b), a relation for i_{dc2} can be derived

$$i_{\mathrm{dc2}}\big|_B = \sqrt{3/2}I_{\mathrm{ph}}\cos\varphi\, d_{\mathrm{cs}}. \tag{13}$$

The above quantity is almost constant for a fixed duty cycle and a constant magnitude of the phase currents (e.g., in the constant-torque region of the traction motor). Hence, the current of the low-voltage source saturates when the MSI operates in condition B.

Ultimately, condition C represents the most undesirable working condition for the converter. The SVM is at the linear modulation limit during the whole control interval T_{cs}, and the

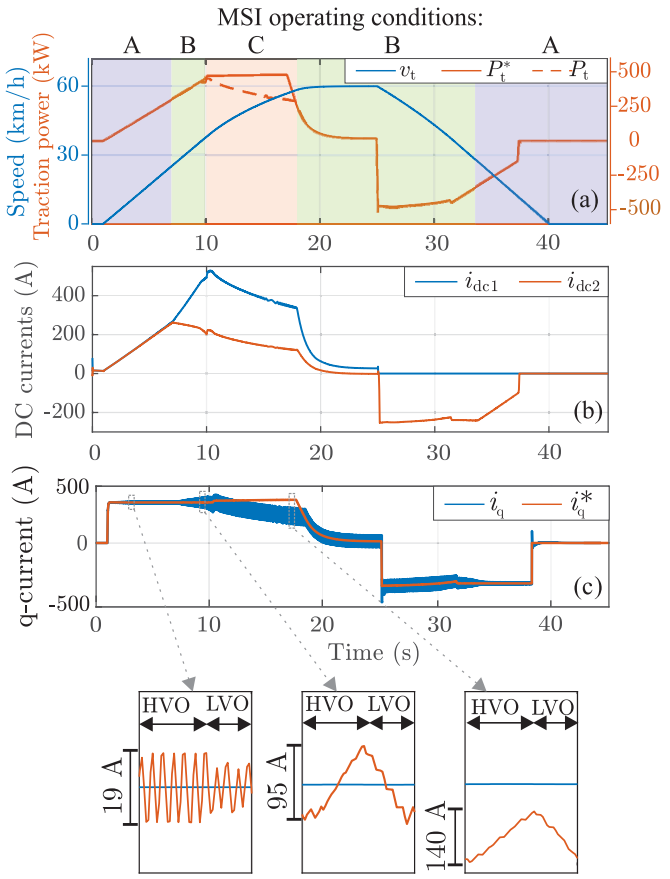

Fig. 4. Simulation results for the analysis of the MSI operating conditions: (a) vehicle speed v_t, power reference P_t^*, and actual traction power P_t of one MSI drive; (b) dc currents; and (c) q-axis current of one MSI drive.

average phase voltage supplied to the motor has an rms value equal to

$$V_{\text{ph}}\big|_C = \frac{V_{\text{dc1}}}{\sqrt{6}}(1 - d_{\text{cs}}) + \frac{V_{\text{dc2}}}{\sqrt{6}} d_{\text{cs}}. \tag{14}$$

This value may be insufficient to keep full control of the motor currents. In such a case, the motor torque and power decrease, and the overall performance of the traction drive is heavily undermined.

Fig. 4 shows simulation results for a case-study tramway vehicle with two MSIs supplied by a 750-V line and a 500-V onboard battery and four traction motors. The voltage level of the battery was specifically chosen below the maximum motor voltage (equal to 620 V) so that all the MSI operating conditions derived above could be observed during the simulation. At low speed, the converter operates in condition A. The dc currents increase proportionally to the traction power according to the value set for d_{cs}. The q-axis current follows its reference with an acceptable ripple at the SVM switching frequency. At medium speed, the MSIs enter working condition B. Due to the switching between LVO and HVO conduction modes, the q-current ripple increases, but the average current error over the entire CSC time window remains zero. Moreover, the power-sharing is no more controlled, and the current of the low-voltage source saturates to a slowly decreasing value. Above the base speed, the motors enter the field-weakening region and the MSIs operate in condition C.

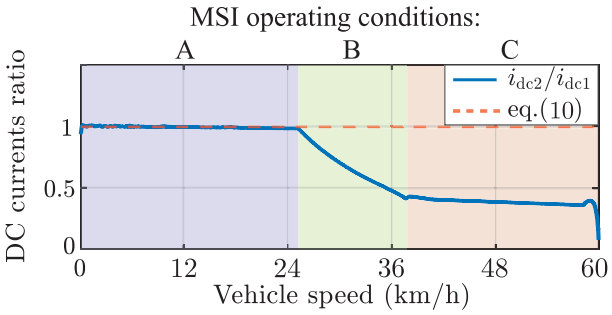

Fig. 5. Ratio between dc currents as a function of the vehicle speed during the simulation for the different operating conditions of the MSI drive.

TABLE II
COMPARISON OF MSI OPERATING MODES

Operating Mode	Motor control	DC sources control
A	Yes	Yes
B	Yes, with increased ripple	No
C	No	No

The q-axis motor current drifts away from its reference and shows a nonacceptable ripple at CSC frequency. The output power falls below its reference, and the dc currents decrease accordingly. When the LRV reaches the speed reference, i.e., during cruising, the torque decreases to a value lower than rated and the converter reenters condition B. At the beginning of the braking phase, the motor requires a high voltage to develop full braking torque, and the converter remains in mode B. As the speed progressively decreases, the motor voltage reduces, and the braking can be completed under operating condition A. However, full regeneration of the braking energy is not always possible in condition B, because the battery voltage is not sufficient. The excess braking power needs to be sent back to the electrified line or dissipated on braking rheostats if the line is not receptive. The ratio between dc currents as a function of simulated vehicle speed is depicted in Fig. 5. Only With the MSI in condition A, the dc currents ratio is controllable and well predicted by the theoretical value derived in (10).

Simulation results prove that, only in condition A, the MSI has full control of the power distribution between dc sources while supplying the motors as required by the vehicle speed profile. The features of the three operating modes of the MSI are summarized in Table II. To keep the system stably in condition A, the voltage level of the onboard storage device must be compatible with the rated voltage of the traction motors. In practice, this condition can be unfeasible for supercapacitors, whose voltage varies significantly with the SOC, while it can be met by battery storage systems, thanks to their flatter voltage to SOC profile.

D. Tradeoff Between Control Resolution and Capacitors Size

Due to the periodic switching between HVO and LVO modes, highly discontinuous currents are drawn from the MSI input terminals. However, the ripple components of these currents are attenuated by the input filters so that smooth

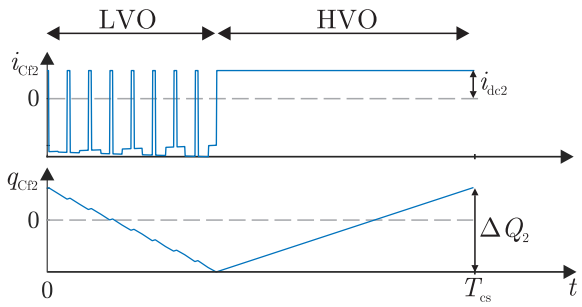

Fig. 6. Ripple current in the low-voltage input capacitor and corresponding moved charge over one CSC time period.

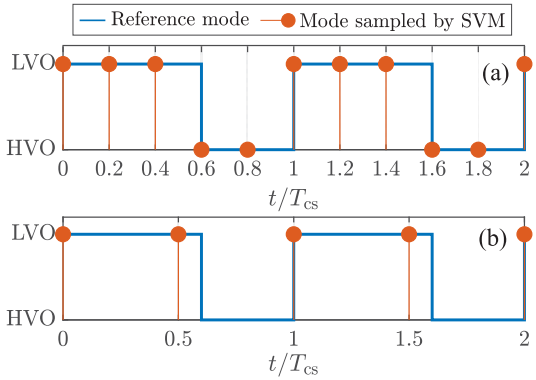

Fig. 7. Effect of the SVM and CSC frequencies on the CSC resolution, for a duty cycle of 0.6: (a) a frequency ratio of 0.2 allows the SVM to operate in LVO and HVO modes for 60% and 40% of the time, respectively, and (b) a coarse frequency of 0.5 determines a wrong operation of the SVM always in the LVO mode.

currents flow in the dc power sources. An LC filter at the line side is already present in LRVs to limit interference with the signaling system, so it can still be designed according to established practices [17]. On the other hand, the capacitor C_{f2} is not present in the standard circuit configuration. The design equation for C_{f2} can be derived from Fig. 6, which represents the ripple component of the input currents i_{in2} (i.e., the capacitor currents) and its time integral (i.e., the charge flowing across the capacitor). During the LVO mode, the low-voltage capacitor current i_{Cf2} has a typical PWM waveform due to SVM operation. During the HVO mode, it is constant and equal to the mean source current i_{dc2}. This profile differs from that found in 2L inverters [39] due to the CSC operation. The resulting moved charge has an almost triangular shape with a peak-to-peak value equal to

$$\Delta Q_2 = C_{f2}\,\Delta V_{Cf2} = i_{dc2}(1-d_{cs})T_{cs}. \tag{15}$$

Substituting (5b) into (15) and rearranging yield

$$C_{f2} = \sqrt{\frac{3}{2}}\frac{m_{LV} I_{ph}\cos\varphi\, d_{cs}(1-d_{cs})}{\Delta V_{Cf2}\, f_{cs}}. \tag{16}$$

The worst case value of capacitance can be obtained by imposing a unit modulation index (i.e., its maximum value), unit power factor, the highest rms value of ac currents, and a CSC duty cycle equal to 0.5

$$C_{f2}^{(max)} = \frac{\sqrt{3}}{8}\frac{\sqrt{2}I_{ph}^{(max)}}{\Delta V_{Cf2}\, f_{cs}}. \tag{17}$$

As expected, a higher CSC frequency results in smaller filter capacitors for a fixed dc voltage ripple and load peak current. Ideally, the upper limit of the CSC frequency would be equal to the switching frequency since the SVM requires a fixed conduction mode in each modulation interval. On the other hand, the ratio between these frequencies determines the resolution of the CSC duty cycle. Indeed, the smallest increment or decrement of d_{cs} is given by

$$\Delta d_{cs} = \frac{f_{cs}}{f_{sw}} = \frac{T_{sw}}{T_{cs}}. \tag{18}$$

This quantization effect on d_{cs} is highlighted in Fig. 7, which refers to a fixed duty cycle of 0.6 and two frequency ratios of 0.2 and 0.5, respectively. In the first case, a resolution of 0.2 is enough for the SVM to correctly operate in LVO and HVO modes for 60% and 40% of the time, respectively. In the second case, a coarse resolution of 0.5 causes the LVO mode to be incorrectly applied for the entire time.

In conclusion, a tradeoff exists between the CSC resolution and the size of the dc filter capacitors. Equation (18) can be employed to select the CSC frequency that gives the desired resolution. Then, for a given ripple of the input current and voltage, (16) can be used to size the input capacitor accordingly.

IV. Stationary Recharge Control

By meeting the constraints highlighted above, the MSI can control the traction motors while regulating the current-sharing between sources with predefined levels of control resolution and ESS current ripple. However, the CSC cannot achieve the controlled recharge of the onboard storage device from the electrified line.

A simple modulation strategy that enables the static recharge can be derived by observing that the MSI can be operated at zero speed as a buck converter with the motor windings used as filter inductors. One leg of the MSI is controlled to switch between V_{dc1} and 0, and the other two legs are permanently connected to V_{dc2}. Specifically, as represented in Fig. 8, s_{11} and s_{21} are driven by the same PWM signal together with their complementary switches s_{31} and s_{41}, while s_{22}, s_{32}, s_{23}, and s_{33} are always ON, and all the other switches are always OFF. By doing so, three dc currents of controllable magnitude can be injected into the motor windings. As clear from direct circuit inspection, the magnitude of the current flowing into the central terminal of one MSI is equal to the sum of the currents of phases 2 and 3, and can be varied by changing the duty cycle of the PWM signal driving s_{11} and s_{21}, and their complementary switches. Since only the first leg is switching, the resulting voltage vector applied to the motors is stationary and so are the phase currents. For this reason, the upper limit of the charging current must correspond to the sum of the maximum magnetizing currents of the motors. The total charging current actually flowing into the onboard source will be the sum of those injected by each MSI drive. It can be controlled by a conventional PI regulator that accepts the current error as input and computes the duty cycle of switches s_{11} and s_{21} of each MSI.

It is worth mentioning that the proposed strategy has a simple interpretation in terms of space vectors of motor

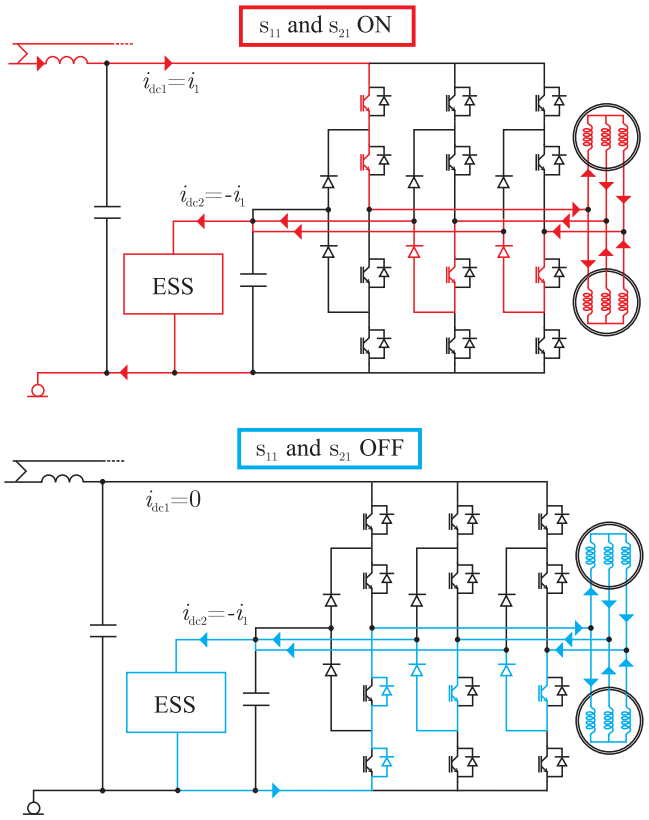

Fig. 8. Switching configurations to operate the MSI as a dc/dc buck converter for the static recharge of the onboard storage device from the overhead line with motor windings used as filter inductors.

voltages and currents. It can be easily verified that the top switching configuration of Fig. 8 corresponds to a motor voltage vector of magnitude $V_{dc1}-V_{dc2}$ laying on the positive α semiaxis, i.e., real and positive; on the other hand, the bottom configuration of Fig. 8 produces a voltage vector of magnitude V_{dc2} laying on the negative α semiaxis, i.e., real and negative. Therefore, the average output voltage vector over a switching period will be real and equal to

$$\boldsymbol{v} = v_\alpha = d(V_1 - V_2) - (1-d)V_2 = dV_1 - V_2 \qquad (19)$$

where d is the duty cycle of s_{11} and s_{21}, i.e., the catenary is connected to the system for a duration of $d \cdot T_s$. The MSI, hence, supplies the motor with an average voltage vector that is real and of controllable magnitude. The resulting space vector $\boldsymbol{i}$ of motor currents will be also real and variable in magnitude because, in dc operation, no displacement between voltages and currents occurs. In particular, $\boldsymbol{i}$ is controlled to be positive so that a set of motor currents flows for which $i_1 > 0$ and $i_2 = i_3 = -i_1/2$. As shown in Fig. 8, the current i_{dc2} is equal to $-i_1$ in both switching configurations. Hence, a negative current of variable magnitude is made to flow continuously into the onboard storage, and the controlled stationary recharge is achieved.

Simulation results for the proposed control are shown in Fig. 9. The charging current is properly controlled to its setpoint. The phase currents in each traction motor are dc with switching ripple determined by the inductance of motor windings. However, this ripple is filtered by the MSI input

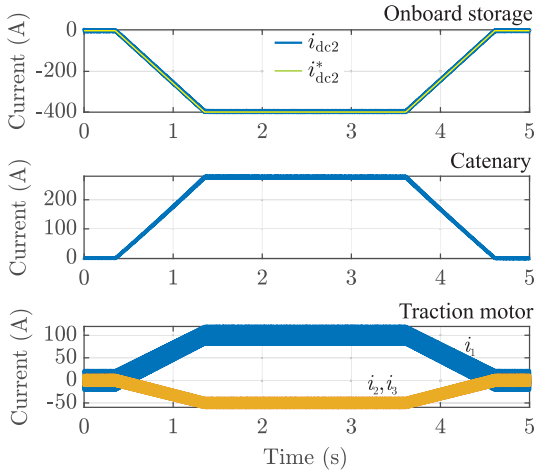

Fig. 9. Simulation results for controlled stationary recharge of the onboard storage device from the catenary through the MSI.

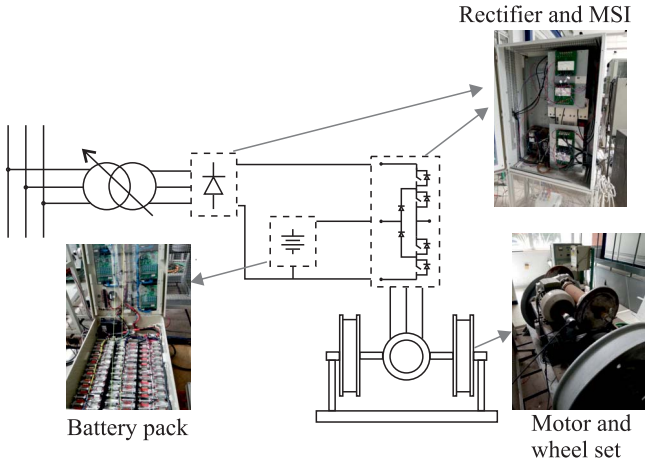

Fig. 10. Test bench layout.

capacitors and does not appear in the currents of the dc sources.

V. Experimental Tests

The theoretical analysis and simulations have been validated by experiments on a small-scale railway test bench. The configuration is shown in Fig. 10, and its main parameters are summarized in Table III.

The system comprises a diode bridge rectifier as a high-voltage source, a battery pack as a low-voltage source, an NPC MSI, and an induction motor connected to the wheels through the gearbox. The control system comprises an field oriented control (FOC) scheme for induction motor control and the CSC scheme for dc power control and was deployed on a real-time dSPACE controller platform.

Three different types of test were carried out:

1) acceleration at fixed CSC duty cycle to validate the analysis of the MSI operating conditions and limits;
2) driving cycle with the MSI always in condition A to assess its full control capability for a dynamic operation of the traction drive;
3) stationary recharge of the battery from the rectifier through the MSI to validate the proposed modulation.

TABLE III
TEST BENCH PARAMETERS

Component	Item	Value
Diode bridge rectifier	Output voltage	350 V
Battery pack	Technology	LiFePo4
	Rated voltage	250 V
	Rated capacity	40 Ah
MSI	SVM frequency	5 kHz
	Current-sharing control frequency	500 Hz
Induction motor (Y-connected)	Rated power	4.2 kW
	Poles	4
	Rated voltage	285 Vrms
	Rated current	11.4 Arms
Wheel set	Transmission ratio	3.26:1
	Wheel diameter	0.90 m
	Equivalent inertia at motor axle	3.7 kgm2

A. Acceleration at Fixed CSC Duty Cycle

During the test, a constant-torque acceleration is requested from the MSI drive. In order to observe all the MSI operating conditions as in the numeric simulations, the battery has a voltage lower than the motor rated voltage, and the CSC duty cycle is fixed. Fig. 11 shows the experimental waveforms of motor speed and q-axis current, rectifier and battery power, and dc currents ratio.

In the early stages of the acceleration, the MSI is in condition A. The q-axis current is stably at its reference, the power output of the two sources increases linearly, and the dc currents follow the ratio dictated by (10) with good approximation. When the MSI enters condition B, the q-axis current is still at its reference but with a sensibly higher ripple at the frequency f_{cs}. The battery power P_{dc2} saturates to an almost constant value, and the slope of the rectifier power P_{dc1} increases subsequently. Hence, no active control of the power split between sources is achieved. The dc currents ratio decreases with the motor speed, as prescribed by (12). Ultimately, working condition C occurs in the last part of the acceleration. The converter loses control over the q-axis current, and the torque decreases to almost zero. The motor finds a working point of equilibrium at an unpredictable speed, and the corresponding power is supplied by the two sources with a noncontrollable ratio.

The effect of the working condition on the motor currents is better shown in Fig. 12(a) and (b), which displays a motor current sampled by a digital oscilloscope in operating conditions A and B, respectively. The current is almost sinusoidal in condition A with a small ripple at the SVM switching frequency and low-order harmonics due to inherent motor nonidealities. On the other hand, it becomes apparently distorted in condition B due to the ripple at 500 Hz introduced by the CSC. On the other hand, Fig. 12(c) shows the current i_{dc1} of the high-voltage source for two CSC frequencies of 500 and 100 Hz, respectively. A decrease of f_{cs} by a factor of five results in an equal increase in the capacitor voltage ripple and, consequently, the source current. This behavior agrees with the sizing equation (16) derived in Section III.

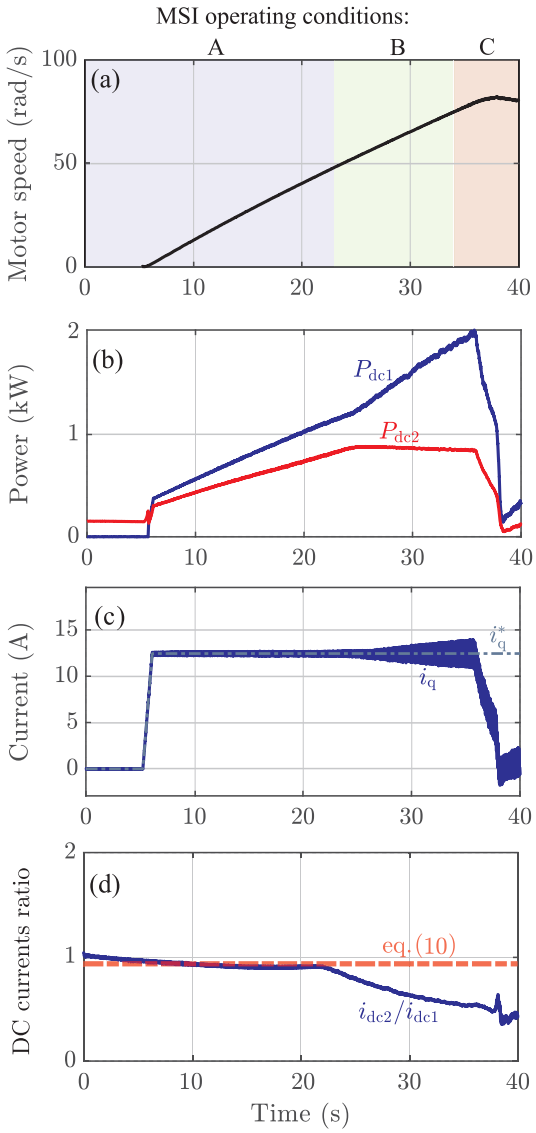

Fig. 11. Experimental results for the acceleration test at fixed CSC duty cycle: (a) motor speed, (b) power output of the two dc sources, (c) q-axis motor current, and (d) ratio between dc currents.

The outcomes of this test confirm that both sources must be at a voltage level compatible with the motor's full voltage for the MSI to avoid working conditions B and C and maintain full control of the entire power system. Such sizing constraint can be met by properly designing the voltage level of the onboard storage system.

B. Full Driving Cycle in Condition A

The only setting of interest for an MSI traction drive is when the converter works stably in condition A and has full control of the motor and source currents. Hence, a driving cycle test is carried out in such condition to assess the performance of the MSI in a real-case operating scenario. In order to keep the MSI always in condition A without replacing the battery with one of higher voltage, the winding connection of the motor is changed from wye to delta.

With the main goal of evaluating the MSI response to variable dc power references, the following EMS is implemented.

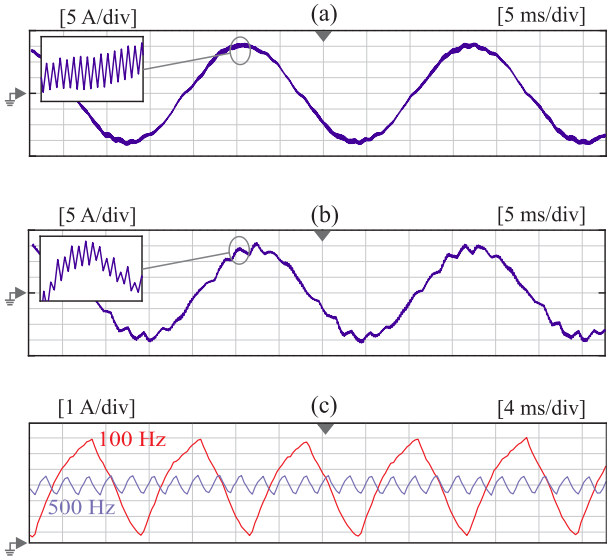

Fig. 12. Oscilloscope acquisitions during the acceleration test: (a) and (b) motor currents with the MSI in conditions A and B, respectively, and (c) rectifier currents with the MSI in condition A for two values of the CSC frequency.

1) *Peak Shaving During Acceleration:* The battery assists the rectifier and limits its power output to a value of 2 kW.
2) *Idle During Cruising:* When the total traction power falls below 2 kW, the battery is disconnected, and the rectifier alone supplies the motor.
3) *Full Regeneration During Braking:* The battery recovers the entire amount of braking energy, and the rectifier is disconnected.

Despite its simplicity, this EMS is fully representative of the considered application and comprises two typical functionalities of a bimode rail traction system: power assist at high loads and full recuperation during electrical braking [40]. The control scheme is as the one in Fig. 3, with the duty cycle d_{cs} computed online through (8b) according to the instantaneous battery power reference set by the EMS controller. In practical applications, the battery SOC is usually controlled at mid-levels to be capable of managing high charging and discharging power values on electrified sections. Before nonelectrified sections, the battery is fully charged and then discharged more deeply on nonelectrified segments to maximize the available energy [17], [41]. A proper design of the capacity considering the maximum catenary-free distance would prevent the storage unit from reaching critical SOC values. However, as the duration of the tests was short compared to the discharge time of the battery pack, an SOC control was judged unnecessary and was not included in the EMS controller.

The results of the test are presented in Fig. 13. During the acceleration, the EMS controller increases the CSC duty cycle to limit the rectifier power output at its predefined threshold. The peak-shaving action is properly carried out by the MSI during both constant-torque and constant-power operations of the motor. It can be noticed that P_{dc2} increases at steps rather than continuously, due to the inherent quantization of the CSC duty cycle that determines a sawtooth-like shape of P_{dc1}.

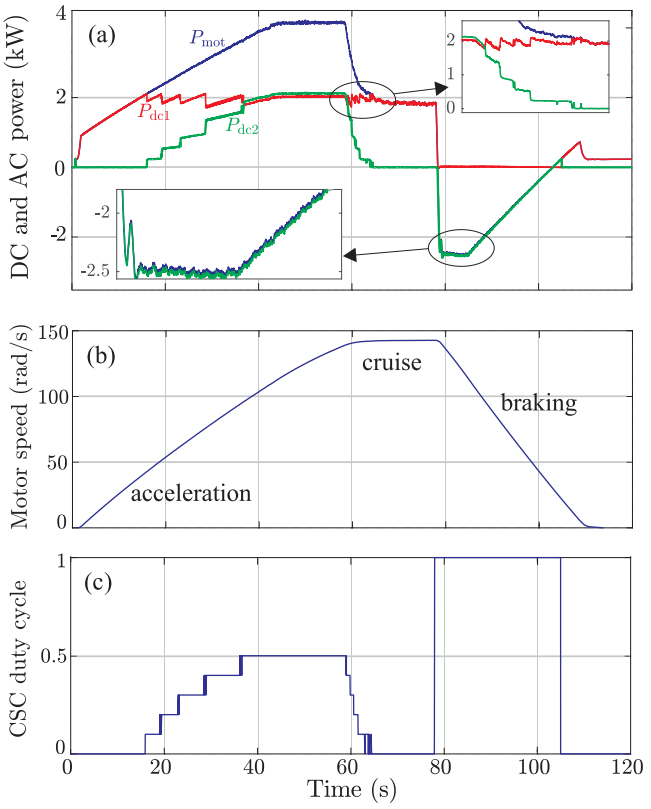

Fig. 13. Experimental results for the full driving cycle test: (a) power output of the motor and dc sources, (b) motor speed, and (c) duty cycle of the CSC.

However, this quantization effect does not significantly affect the system performance, thanks to a good 10% CSC resolution achieved by choosing a current-sharing frequency of 500 Hz. When cruising begins, the battery power rapidly falls toward zero with a similar step-by-step profile, and the rectifier acts as the only power source. Finally, braking starts: the CSC duty cycle is increased to unity by the EMS controller, and full braking energy recovery is effectively achieved by the battery.

The results confirm that, with a proper design of the battery voltage level with respect to the motor rated voltage, the CSC is able to operate the MSI drive for the twofold task of motor control and energy management of the sources.

C. Battery Stationary Recharge

The experimental results of the stationary recharge test are shown in Fig. 14. The battery current i_{dc2} is properly controlled at the reference value of -10 A for 20 s. The current of the first motor phase i_1 has the same mean value of i_{dc2}, while that of the second phase current i_2 is negative and halved. The motor currents exhibit a negligible ripple at switching frequency. The dc currents also show the 300-Hz ripple introduced by the rectifier due to the absence of an input filter. In real applications, this ripple would be filtered by the line input choke.

The results confirm the validity of the proposed modulation to exploit the motor windings as filter inductors and achieve a controlled recharge of the battery from the electrified line through the MSI at a motor standstill.

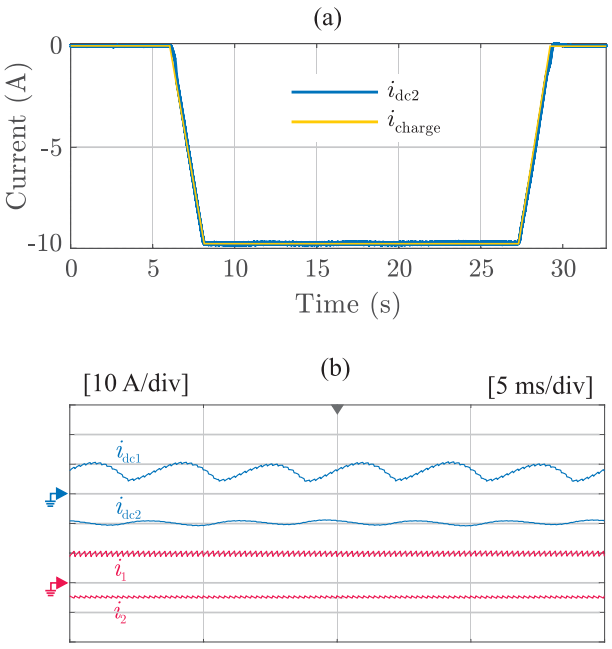

Fig. 14. Experimental results for the stationary battery recharge test: (a) battery current and its reference and (b) oscilloscope acquisitions of dc sources and motor currents.

VI. Conclusion

This article has addressed the application of NPC-based MSIs to traction systems of multimode rail vehicles to reduce the number of converters used in traditional topologies.

First, the equations describing the converter behavior under its state-of-the-art control have been derived to understand the features and limits of the considered power architecture. The analysis showed that the MSI traction drive can operate in three different conditions, depending on the motor operating point and the voltage level of the dc inputs. Among these conditions, only one guarantees full control of the motors and the dc currents. This condition is achieved when the voltage of the dc sources is sufficient for the motor-rated voltage. This, in turn, results in a constraint on the design process of the onboard storage device in MSI-based architectures. The theoretical analysis also revealed that the control of the dc currents is affected by an inherent quantization so that the output power of each source can be varied only in discrete steps. This quantization can be made finer by decreasing the frequency of the CSC at the price of the increased size of the input filter capacitors.

Second, a novel modulation strategy has been proposed to control the MSI for the stationary charging of the onboard storage from the electrified line. In the proposed strategy, the MSI is operated as a buck converter by using the motor windings as filter inductors, which is effective when the rail vehicle is stationary, for example, at stations and depots.

In conclusion, by observing the highlighted design constraints and complementing the baseline CSC with the proposed stationary recharge control, the MSI can be operated to match all the typical functionalities of a multimode rail traction circuit with the advantage of a reduced number of power converters. This is regarded as a promising result and motivates further research efforts on this converter concept with application to multimode traction systems, where volume and weight reductions are key objectives for designers.

References

[1] T. Ratniyomchai, S. Hillmansen, and P. Tricoli, "Recent developments and applications of energy storage devices in electrified railways," *IET Elect. Syst. Transp.*, vol. 4, no. 1, pp. 9–20, Mar. 2014.

[2] E. Fedele, D. Iannuzzi, and A. D. Pizzo, "Onboard energy storage in rail transport: Review of real applications and techno-economic assessments," *IET Electr. Syst. Transp.*, vol. 11, no. 4, pp. 279–309, Dec. 2021.

[3] A. González-Gil, R. Palacin, and P. Batty, "Sustainable urban rail systems: Strategies and technologies for optimal management of regenerative braking energy," *Energy Convers. Manag.*, vol. 75, pp. 374–388, Nov. 2013.

[4] P. Ralon, M. Taylor, A. Ilas, H. Diaz-Bone, and K.-P. Kairies, "Electricity storage and renewables: Costs and markets to 2030," IRENA, Abu Dhabi, UAE, Tech. Rep., Oct. 2017. [Online]. Available: https://www.irena.org/publications/2017/Oct/Electricity-storage-and-renewables-costs-and-markets

[5] C. Wu, W. Zhang, S. Lu, Z. Tan, F. Xue, and J. Yang, "Train speed trajectory optimization with on-board energy storage device," *IEEE Trans. Intell. Transp. Syst.*, vol. 20, no. 11, pp. 4092–4102, Nov. 2019.

[6] C. Wu, S. Lu, F. Xue, L. Jiang, and M. Chen, "Optimal sizing of onboard energy storage devices for electrified railway systems," *IEEE Trans. Transport. Electrific.*, vol. 6, no. 3, pp. 1301–1311, Sep. 2020.

[7] L. P. Di Noia, F. Genduso, R. Miceli, and R. Rizzo, "Optimal integration of hybrid supercapacitor and IPT system for a free-catenary tramway," *IEEE Trans. Ind. Appl.*, vol. 55, no. 1, pp. 794–801, Jan. 2019.

[8] M. Ogasa and Y. Taguchi, "Development of contact-wire/battery hybrid LRV hybrid technology with lithium ion rechargeable battery for LRV," in *Proc. IEEE Vehicle Power Propuls. Conf.*, Piscataway, NJ, USA, Sep. 2010, pp. 1–6.

[9] Y. Kono, N. Shiraki, H. Yokoyama, and R. Furuta, "Catenary and storage battery hybrid system for electric railcar series EV-E301," in *Proc. Int. Power Electron. Conf. (IPEC)*, May 2014, pp. 2120–2125.

[10] H. Ozawa and T. Ogihara, "Running test of contactwire-less tramcar using lithium ion battery," *IEEJ Trans. Electr. Electron. Eng.*, vol. 3, no. 3, pp. 360–362, Apr. 2008.

[11] F. Becker and A. Dammig, "Catenary free operation of light rail vehicles—Topology and operational concept," in *Proc. 18th Eur. Conf. Power Electron. Appl. (EPE ECCE Europe)*, Sep. 2016, pp. 1–10.

[12] J. F. Reynaud, M. Garmendia, and T. Nieva, "Comprehensive integration of onboard energy storage systems in tramways: Birmingham tram case study," in *Proc. IEEE Int. Conf. Elect. Syst. Aircr., Railway, Ship Propuls. Road Vehicles Int. Transp. Electrific. Conf. (ESARS-ITEC)*, Nov. 2018, pp. 1–6.

[13] M. Meinert, "New mobile energy storage system for rolling stock," in *Proc. 13th Eur. Conf. Power Electron. Appl.*, Piscataway, NJ, USA, 2009, pp. 1–10.

[14] Z. X. Liu, Q. Y. Bu, W. R. Chen, Q. Li, M. Li, and B. C. Sun, "Fuel cell based hybrid power system design for a passenger tram," in *Proc. 21st World Hydrogen Energy Conf. (WHEC)*, 2016, vol. 51, no. 3, pp. 1119–1121.

[15] F. Peng *et al.*, "Development of master-slave energy management strategy based on fuzzy logic hysteresis state machine and differential power processing compensation for a PEMFC-LIB-SC hybrid tramway," *Appl. Energy*, vol. 206, pp. 346–363, Nov. 2017.

[16] K. Tokuyama, M. Shimada, K. Terasawa, and T. Kaneko, "Practical application of a hybrid drive system for reducing environmental load," *Hitachi Rev.*, vol. 57, pp. 23–27, Mar. 2008.

[17] G. Abad, *Power Electronics and Electric Drives for Traction Applications*. Chichester, U.K.: Wiley, 2016.

[18] H. J. Ahmad and M. Hagiwara, "A compact high-power noninverting bidirectional buck–boost chopper for onboard battery energy storage systems," *IEEE Trans. Power Electron.*, vol. 37, no. 2, pp. 1722–1735, Feb. 2022.

[19] A. Rujas, V. M. Lopez, A. Garcia-Bediaga, A. Berasategi, and T. Nieva, "Influence of SiC technology in a railway traction DC-DC converter design evolution," in *Proc. IEEE Energy Convers. Congr. Expo. (ECCE)*, Oct. 2017, pp. 931–938.

[20] G. Liu, Y. Wu, K. Li, Y. Wang, and C. Li, "Development of high power SiC devices for rail traction power systems," *J. Cryst. Growth*, vol. 507, pp. 442–452, Feb. 2019.

[21] D. Yildirim *et al.*, "Full-scale physical simulator of all SiC traction motor drive with onboard supercapacitor ESS for light-rail public transportation," *IEEE Trans. Ind. Electron.*, vol. 67, no. 8, pp. 6290–6301, Aug. 2020.
[22] M. Hagiwara, K. Nishimura, and H. Akagi, "A medium-voltage motor drive with a modular multilevel PWM inverter," *IEEE Trans. Power Electron.*, vol. 25, no. 7, pp. 1786–1799, Jul. 2010.
[23] N. Mukherjee and P. Tricoli, "A new state of charge control of modular multilevel converters with supercapacitors for traction drives," in *Proc. IEEE Energy Convers. Congr. Expo. (ECCE)*, Sep. 2015, pp. 3674–3680.
[24] M. Coppola, A. D. Pizzo, and D. Iannuzzi, "A power traction converter based on modular multilevel architecture integrated with energy storage devices," in *Proc. Electr. Syst. Aircr., Railway Ship Propuls.*, Oct. 2012, pp. 1–7.
[25] C. Gan, Q. Sun, J. Wu, W. Kong, C. Shi, and Y. Hu, "MMC-based SRM drives with decentralized battery energy storage system for hybrid electric vehicles," *IEEE Trans. Power Electron.*, vol. 34, no. 3, pp. 2608–2621, Mar. 2019.
[26] J. Anzola *et al.*, "Review of architectures based on partial power processing for DC-DC applications," *IEEE Access*, vol. 8, pp. 103405–103418, 2020.
[27] F. Yang, H. Ge, Z. Yu, Y. Li, and H. Wu, "Topology and control of four-quadrant dual-DC-port dual-buck inverters for semi-two-stage DC-AC power conversion," *IEEE Trans. Ind. Electron.*, vol. 68, no. 11, pp. 10718–10729, Nov. 2021.
[28] H. J. Ahmad and M. Hagiwara, "Interleaved bidirectional chopper with auxiliary converters for DC electric railways," *IEEE Trans. Power Electron.*, vol. 36, no. 5, pp. 5336–5347, May 2021.
[29] M. G. Varzaneh, A. Rajaei, M. Forouzesh, Y. P. Siwakoti, and F. Blaabjerg, "A single-stage multi-port buck-boost inverter," *IEEE Trans. Power Electron.*, vol. 36, no. 7, pp. 7769–7782, Jul. 2021.
[30] M. G. Varzaneh, A. Rajaei, A. Jolfaei, and M. R. Khosravi, "A high step-up dual-source three-phase inverter topology with decoupled and reliable control algorithm," *IEEE Trans. Ind. Appl.*, vol. 56, no. 4, pp. 4501–4509, Aug. 2020.
[31] F. Yang, H. Ge, J. Yang, R. Dang, and H. Wu, "A family of dual-buck inverters with an extended low-voltage DC-input port for efficiency improvement based on dual-input pulsating voltage-source cells," *IEEE Trans. Power Electron.*, vol. 33, no. 4, pp. 3115–3128, Apr. 2018.
[32] L. Dorn-Gomba, P. Magne, B. Danen, and A. Emadi, "On the concept of the multi-source inverter for hybrid electric vehicle powertrains," *IEEE Trans. Power Electron.*, vol. 33, no. 9, pp. 7376–7386, Sep. 2018.
[33] L. Dorn-Gomba, E. Chemali, and A. Emadi, "A novel hybrid energy storage system using the multi-source inverter," in *Proc. IEEE Appl. Power Electron. Conf. Expo. (APEC)*, Mar. 2018, pp. 684–691.
[34] L. Dorn-Gomba, J. Guo, and A. Emadi, "Multi-source inverter for power-split hybrid electric powertrains," *IEEE Trans. Veh. Technol.*, vol. 68, no. 7, pp. 6481–6494, Jul. 2019.
[35] O. Salari, K. H. Zaad, A. Bakhshai, and P. Jain, "Reconfigurable hybrid energy storage system for an electric vehicle DC-AC inverter," *IEEE Trans. Power Electron.*, vol. 35, no. 12, pp. 12846–12860, Dec. 2020.
[36] M. Chymera, A. C. Renfrew, M. Barnes, and J. Holden, "Simplified power converter for integrated traction energy storage," *IEEE Trans. Veh. Technol.*, vol. 60, no. 4, pp. 1374–1383, May 2011.
[37] J. Ebrahimi, O. Salari, S. Eren, K. Hashtrudi-Zaad, A. Bakhshai, and P. Jain, "Efficiency improved multi-source inverter for hybrid energy storage systems in electric vehicle application," *IEEE Trans. Power Electron.*, vol. 37, no. 2, pp. 1982–1997, Feb. 2022.
[38] (2018). *Electric Multiple Units*. [Online]. Available: https://new.abb.com/power-converters-inverters/traction-converters/compact-converters/bordline-cc-for-electrical-multiple-units
[39] P. A. Dahono, Y. Sato, and T. Kataoka, "Analysis and minimization of ripple components of input current and voltage of PWM inverters," *IEEE Trans. Ind. Appl.*, vol. 32, no. 4, pp. 945–950, Jul. 1996.
[40] L. Grigans and L. Latkovskis, "Study of control strategies for energy storage system on board of urban electric vehicles," in *Proc. 14th Int. Power Electron. Motion Control Conf. (EPE-PEMC)*, Sep. 2010, p. T9-34.
[41] M. Ogasa and Y. Taguchi, "Power electronics technologies for a lithium ion battery tram," in *Proc. Power Convers. Conf.*, Nagoya, Japan, Apr. 2007, pp. 1369–1375.

Emanuele Fedele received the B.Sc. and M.Sc. degrees in electrical engineering from the Department of Electrical Engineering and Information Technology, University of Naples Federico II, Naples, Italy, in 2015 and 2018, respectively, where he is currently pursuing the Ph.D. degree in electrical engineering.

His research interests include modeling and control of power electronics, and electrical drives for traction systems.

Diego Iannuzzi was born in Naples, Italy, in 1972. He received the M.Sc. *(cum laude)* and Ph.D. degrees in electrical engineering from the University of Naples Federico II, Naples, Italy, in 1998 and 2001, respectively.

He was a Visiting Professor with the University of South Carolina, Columbia, SC, USA, the École polytechnique fédérale de Lausanne (EPFL), Lausanne, Switzerland, the Institut National Polytechnique, Toulouse, France, and the Polytechnic of Milan, Milan, Italy, where he was involved in the field of electrical drives for traction applications. He has been with the Traction Competence Centre of Campania, Naples, since 2004, where he was involved in research activities. He has been an Associate Professor with the Department of Electrical Engineering, University of Naples Federico II, since 2005.

Pietro Tricoli (Member, IEEE) was born in Naples, Italy, in September 8, 1978. He received the M.S. *(cum laude)* and Ph.D. degrees in electrical engineering from the University of Naples Federico II, Naples, in 2002 and 2005, respectively.

He was a Visiting Scholar with the Department of Electrical and Computer Engineering, University of Wisconsin-Madison, Madison, WI, USA, in 2005. In 2006, he was also a Visiting Scholar with the Department of Electrical and Electronic Engineering, Nagasaki University, Nagasaki, Japan. From 2006 to 2011, he was a Post-Doctoral Research Fellow with the Department of Electrical Engineering, University of Naples Federico II. In 2011, he moved to the Department of Electronic, Electrical, and Systems Engineering, University of Birmingham, Birmingham, U.K., as a Lecturer. He was promoted to Senior Lecturer in 2017 and to Reader in Power Electronics Systems in 2021. He has authored more than 100 scientific papers published in international journals and conference proceedings. His research interests include storage devices for road electric vehicles, railways, and rapid transit systems, wind and photovoltaic generation, railway electrification systems, and modeling and control of multilevel converters.

Dr. Tricoli is a member of the IEEE Industrial Electronics Society and the Energy Institute. He is the Web and Publication Chair of the International Conference on Clean Electrical Power. He is also the Deputy Editor-in-Chief and a Feature Editor of the *IET Journal Renewable Power Generation*. He is a Registered Professional Engineer in Italy.

Andrea Del Pizzo (Member, IEEE) received the M.S. degree in electrical engineering from the University of Naples Federico II, Naples, Italy, in 1979.

He became an Assistant Professor in 1983 and a Full Professor of electrical machines and drives in 2001 at the University of Naples Federico II. He was a Contract Professor with the University of Cassino, Cassino, Italy, and the University of Sannio RCOST, Benevento, Italy. Since 2013, he has been the Head of the Research Center on Electric Propulsion of Land, Sea, and Air Vehicles, University of Naples Federico II. He has been responsible and/or a coordinator of many research projects, including private companies and public research institutions. His main research interests include modeling electrical machines and drives, high-performance permanent-magnet brushless and induction motor drives, modular multilevel converters, and high-power-density drives for electric propulsion.

Prof. Del Pizzo is also a General Co-Chairman of the International Conference on Power Electronics and Electrical Drives.